Computers and Mathematics with Applications 77 (2019) 1255–1272

Contents lists available at ScienceDirect

Computers and Mathematics with Applications

journal homepage: www.elsevier.com/locate/camwa

Total variation and high-order total variation adaptive model for restoring blurred images with Cauchy noise

Jing-Hua Yang [a], Xi-Le Zhao [a,*], Jin-Jin Mei [b], Si Wang [a], Tian-Hui Ma [c], Ting-Zhu Huang [a]

[a] School of Mathematical Sciences, University of Electronic Science and Technology of China, Chengdu, Sichuan, 611731, PR China
[b] School of Mathematics and Statistics, Fuyang Normal University, Fuyang, Anhui 236037, PR China
[c] School of Mathematics and Statistics, Xi'an Jiaotong University, Xi'an, Shaanxi 710049, PR China

ARTICLE INFO

Article history:
Received 26 March 2018
Received in revised form 25 September 2018
Accepted 3 November 2018
Available online 5 December 2018

Keywords:
Cauchy noise
Total variation and high-order total variation
Adaptive regularization parameters
Alternating direction method of multipliers
Image restoration

ABSTRACT

In this paper, we propose a novel model to restore an image corrupted by blur and Cauchy noise. The model is composed of a data fidelity term and two regularization terms including total variation and high-order total variation. Total variation provides well-preserved edge features, but suffers from staircase effects in smooth regions, whereas high-order total variation can alleviate staircase effects. Moreover, we introduce a strategy for adaptively selecting regularization parameters. We develop an efficient alternating minimization algorithm for solving the proposed model. Numerical examples suggest that the proposed method has the advantages of better preserving edges and reducing staircase effects.

1. Introduction

Image restoration is an important issue in many engineering fields [1–7]. Most existing image denoising techniques handle the restoration of images corrupted by additive Gaussian noise [8–10], multiplicative noise [11–13], and impulse noise [14,15]. But there are other types of noise in practical applications, such as Cauchy noise, Rician noise, and Gamma noise. In this paper, we aim at restoring images corrupted by blur and Cauchy noise, which exists widely in biomedical images and synthetic aperture radar images [16,17]. Mathematically, the degradation process can be described as

$$f = Ku + v, \tag{1}$$

where $f \in \mathbb{R}^{m\times n}$ is the degraded image, $u \in \mathbb{R}^{m\times n}$ is the original image, K is a linear blur operator, v is the Cauchy noise with a probability density function [18]

$$g(v) = \frac{1}{\pi}\frac{\gamma}{\gamma^2 + (v-\sigma)^2}, \tag{2}$$

where $\gamma > 0$ is the scale parameter and $\sigma \in R$ is the localization parameter. Without loss of generality, in the following discussion we consider $\sigma = 0$.

* Corresponding author.
E-mail addresses: yangjinghua110@126.com (J.-H. Yang), xlzhao122003@163.com (X.-L. Zhao), meijinjin666@126.com (J.-J. Mei), uestcsiwang@163.com (S. Wang), nkmth0307@126.com (T.-H. Ma), tingzhuhuang@126.com (T.-Z. Huang).

https://doi.org/10.1016/j.camwa.2018.11.003
0898-1221/

There exist many methods for Cauchy noise removal. Achim and Euruoglu [19] removed Cauchy noise via a bivariate maximum a posteriori estimator in the complex wavelet domain. Chang et al. [20] studied a recursive restoration algorithm based on Markov random field model to restore images under Cauchy noise. Nikolova [21] removed Cauchy noise in RGB color images using an image segmentation method with the improved quality of segmentation and Cauchy noise reduction. Due to the fact that total variation (TV) [22,23] can preserve sharp image edges, Sciacchitano et al. [18] proposed the following TV-based Cauchy denoising and deblurring model:

$$\arg\min_u \alpha\|Du\|_1 + \frac{1}{2}\big(\langle \log(\gamma^2 + (Ku - f)^2), \mathbf{1}\rangle_X + \mu\|Ku - u_0\|_F^2\big), \tag{3}$$

where $\|Du\|_1$ is the TV regularization term (see Section 2.1), the second term is the data fidelity term based on Cauchy distribution, the third term is a quadratic penalty term to ensure the convexity of the model (3), $\langle\cdot,\cdot\rangle_X$ denotes the standard inner product, the logarithmic function log is pixel-by-pixel, $\alpha > 0$ is a regularization parameter, K denotes a linear blurring operator, $\mathbf{1}$ is an m-by-n matrix of ones, μ is a positive penalty parameter, and u_0 is the pre-denoising result of the median filter [24]. The model (3) pushes the solution close to the pre-denoising result, but the median filter does not always provide a satisfactory result. So Mei et al. [25] studied the non-convex model by removing the third term in (3). They used the alternating direction method of multipliers (ADMM) to solve the non-convex optimization problem with promising results. However, since the data fidelity term is non-convex, the solution strongly depends on initializations and solving schemes. TV regularization can preserve fine features and sharp edges, but it often produces staircase artifacts and false edges which do not exist in the true images [26–29]. In many applications, some authors proposed methods combining TV and high-order TV to reduce staircase artifacts [30–37].

Due to the fact that the image distribution is inhomogeneous, in terms of cartoon and texture, global constant regularization parameters do not satisfy local piecewise smoothness constraints in all local image regions [38,39]. Therefore, some works considered adjusting the spatially dependent regularization parameters adaptively [40–47]. Liao et al. [44] used generalized cross-validation [48] to choose the regularization parameters adaptively. Chen et al. [45,46] proposed discrepancy rule-based methods for parameter selections, which rely on a good estimate of the noise level. Ma et al. [40] proposed a method to simultaneously estimate the restored image and regularization parameters, where regularization parameters become more reasonable by exploiting the more accuracy restored image instead of the observed image.

In this paper, we propose a new adaptive model combining TV and high-order TV regularization for restoring blurred images with Cauchy noise (see Section 3). In the proposed model, regularization parameters are selected adaptively. In texture areas, TV regularization preserves sharp edges; whereas in flat areas, the high-order TV regularization maintains the smoothness. Numerically, we develop an efficient iterative algorithm for solving the proposed model. The proposed algorithm can adaptively select the values of regularization parameters to balance the data fidelity and regularization terms. Experimental results demonstrate that the proposed method is competitive with the state-of-the-art methods.

The remainder of this paper is organized as follows. In Section 2, we present some preliminaries used in our method. The TV and high-order TV adaptive model is described in Section 3. In Section 4, we provide an efficient alternating minimization algorithm for solving the proposed model and discuss the convergence of the proposed algorithm. In Section 5, we present extensive experimental results to illustrate the effectiveness of the proposed method. In Section 6, we conclude this paper.

2. Preliminary

In this section, we give some preliminaries and review the framework of ADMM.

2.1. Notations

For the sake of simplicity, we focus on gray images and assume that images are periodically extended. We denote an image u as an $m \times n$ matrix, where $u_{i,j}$ represents the intensity value of u at pixel (i, j) for $i = 1, 2, \ldots, m, j = 1, 2, \ldots, n$. In the rest of this paper, we let $\|\cdot\|_2$, $\|\cdot\|_F$, and $\circ$ denote the 2-norm, the Frobenius norm, and the Hadamard product, respectively. Let X be the Euclidean space $R^{m\times n}$, $\langle\cdot,\cdot\rangle_X$ and $\|\cdot\|_X$ be the inner product and the Euclidean norm, respectively. Denote by Y the space $X \times X$ equipped with the inner product $\langle\cdot,\cdot\rangle_Y$. Similarly, we denote the space $Y \times Y$ as Z. $\langle\cdot,\cdot\rangle_Z$ and $\|\cdot\|_Z$, respectively, denote the inner product and the norm. For $p = (p^1, p^2) \in Y$ and $q = (q^1, q^2) \in Y$, we have

$$\|p\|_Y = \sqrt{\langle p, p\rangle_Y}, \qquad \langle p, q\rangle_Y = \langle p^1, q^1\rangle_X + \langle p^2, q^2\rangle_X.$$

Moreover, for $y = (y^1, y^2) \in Y$, $|y|$ denotes the $m \times n$ matrix whose element $|y|_{i,j}$ is equal to $\|y_{i,j}\|_2$ with $y_{i,j} = (y^1_{i,j}, y^2_{i,j})$.

For $u \in X$, we introduce the following discrete forward and backward difference operators:

$$(\mathcal{D}_x^+ u)_{i,j} = \begin{cases} u_{i,j+1} - u_{i,j}, & 1 \le j \le n-1, \\ u_{i,1} - u_{i,n}, & j = n, \end{cases}$$

$$(\mathcal{D}_y^+ u)_{i,j} = \begin{cases} u_{i+1,j} - u_{i,j}, & 1 \le i \le m-1, \\ u_{1,j} - u_{n,j}, & i = m, \end{cases}$$

$$(\mathcal{D}_x^- u)_{i,j} = \begin{cases} u_{i,1} - u_{i,n}, & j = 1, \\ u_{i,j} - u_{i,j-1}, & 2 \le j \le n, \end{cases}$$
$$(\mathcal{D}_y^- u)_{i,j} = \begin{cases} u_{1,j} - u_{n,j}, & i = 1, \\ u_{i,j} - u_{i-1,j}, & 2 \le i \le m, \end{cases}$$
$$(D_{xx}^{-+} u)_{i,j} = (D_x^- (D_x^+ u))_{i,j},$$
$$(D_{yy}^{+-} u)_{i,j} = (D_y^+ (D_y^- u))_{i,j}.$$

Other second-order difference operators $D_{xx}^{+-}u$, $D_{xy}^{++}u$, $D_{yx}^{++}u$, $D_{yy}^{-+}u$, and $D_{yx}^{--}u$ can be similarly defined. Periodic boundary conditions are used in the forward and backward difference schemes, and then the fast Fourier transform can be adopted in the proposed algorithm.

The discrete TV and high-order TV of u are defined as

$$\|Du\|_1 = \sum_{1\le i\le m, 1\le j\le n} |Du|_{i,j}, \qquad Du = (D_x^+ u, D_y^+ u).$$
$$\|D^2 u\|_1 = \sum_{1\le i\le m, 1\le j\le n} |D^2 u|_{i,j}, \qquad D^2 u = \begin{pmatrix} D_{xx}^{-+} u & D_{xy}^{++} u \\ D_{yx}^{++} u & D_{yy}^{-+} u \end{pmatrix}.$$
$$|Du|_{i,j} = \sqrt{(D_x^+ u)_{i,j}^2 + (D_y^+ u)_{i,j}^2},$$
$$|D^2 u|_{i,j} = \sqrt{(D_{xx}^{-+} u)_{i,j}^2 + (D_{xy}^{++} u)_{i,j}^2 + (D_{yx}^{++} u)_{i,j}^2 + (D_{yy}^{-+} u)_{i,j}^2}.$$

Using the inner products of X, Y, and Z, we can find that the discrete divergence operators $D^* : Y \to X$ and $(D^2)^* : Z \to X$ are given as follows:

$$\langle D^* y, u\rangle_X = \langle y, -Du\rangle_Y, \qquad \langle (D^2)^* z, u\rangle_X = \langle z, D^2 u\rangle_Z,$$

where $u \in X$, $y \in Y$, and $z \in Z$. Then they are formulated as follows:

$$D^* y = D_x^- y^1 + D_y^- y^2,$$

$$(D^2)^* z = D_{xx}^{+-} z^{11} + D_{yx}^{--} z^{12} + D_{xy}^{--} z^{21} + D_{yy}^{+-} z^{22}.$$

Finally, the composite operators D^*D and $(D^2)^* D^2$ are used in the following section.

2.2. ADMM algorithm

The ADMM [49–51] solves optimization problems with the following form:

$$\begin{aligned} &\arg\min_{x,y} f(x) + g(y), \\ s.t.\quad &Ax + By = b, \quad x, y \in X, \end{aligned} \tag{4}$$

where $f: \mathbb{R}^n \to \mathbb{R}$ and $g: \mathbb{R}^n \to \mathbb{R}$ are convex functions, $X \subseteq \mathbb{R}^n$ is a closed convex set, $A \in \mathbb{R}^{l\times n}$ and $B \in \mathbb{R}^{l\times n}$ are given matrices, and $b \in \mathbb{R}^l$ is a given vector. The augmented Lagrangian function of (4) is

$$L(x, y, z) = f(x) + g(y) + \frac{\beta}{2}\|Ax + By - b - z\|_2^2, \tag{5}$$

where z is the Lagrangian multiplier and β is a penalty parameter. The iterations of ADMM are given in **Algorithm** 1.

Algorithm 1: ADMM for solving the optimization problem (4).

Input: $\beta > 0$.
Initialize: y^0 and z^0.
1: **for** $k = 0$ to K **do**
2: $x^{k+1} = \arg\min_x L(x, y^k, z^k)$,
3: $y^{k+1} = \arg\min_y L(x^{k+1}, y, z^k)$,
4: $z^{k+1} = z^k - (Ax^{k+1} + By^{k+1} - b)$.
5: **end for**
Output: x, y.

3. Adaptive TV and high-order TV model

Considering the advantages of TV and high-order TV, we combine TV with high-order TV regularization as follows:

$$\arg\min_u \|g_1 \circ Du\|_1 + \|g_2 \circ D^2u\|_1 + \frac{1}{2}\big(\langle \log(\gamma^2 + (Ku-f)^2), \mathbf{1}\rangle_X + \mu\|Ku-u_0\|_X^2\big), \tag{6}$$

where $\circ$ denotes the element-wise multiplication, $g_1 \in \mathbb{R}^{m\times n}$ and $g_2 \in \mathbb{R}^{m\times n}$ are spatially dependent regularization parameters, Du and D^2u denote the first-order and high-order difference matrices, respectively. This model is able to preserve edges while reducing staircase effects in smooth regions.

In [40], the authors proposed a general model to adjust regularization parameters. The advantage is that regularization parameters and the restored image can benefit from each other until joint optimization, for more details see [40]. Similarly, we form a spatially adaptive regularization parameters selection model. It has the form

$$\arg\min_{u,g_1,g_2} E(u,g_1,g_2) = F_1(u) + F_2(g_1,g_2) + R(u,g_1,g_2), \tag{7}$$

where $F_1(u)$ and $F_2(g_1,g_2)$ are fidelity terms for the restored image and regularization parameters. g_1 and g_2 denote spatially dependent regularization parameters. $R(u,g_1,g_2)$ is a regularizer. Regularization parameters are changing more reasonably by exploiting the restored image u.

Combining (6) and (7), finally we propose the following model for restoring the blurred image with Cauchy noise, which adjusts regularization parameters adaptively:

$$\begin{aligned}\arg\min_{u,g_1,g_2} E(u,g_1,g_2) =& \frac{1}{2}\big(\langle \log(\gamma^2 + (Ku-f)^2), \mathbf{1}\rangle_X + \mu\|Ku-u_0\|_X^2\big) + \alpha\big(\|g_1 - \frac{M}{\alpha}\cdot\mathbf{1}\|_X^2 + \|g_2 - \frac{M}{\alpha}\cdot\mathbf{1}\|_X^2\big)\\ &+ \sum_{1\le i\le m,1\le j\le n} (g_1)_{i,j}^2 (H_r(|Du|))_{i,j} + \sum_{1\le i\le m,1\le j\le n} (g_2)_{i,j}^2 (H_r(|D^2u|))_{i,j},\end{aligned} \tag{8}$$

where α and M are positive parameters, H_r denotes a discrete mean filter with window size r (with a periodic extension at the boundary).

Now we analyze the numerical behavior of the solution. The following result shows the existence of the solution of the minimization problem (8).

Theorem 3.1. *If $\alpha > 0, M > 0, f \in X$, and $Null(K) \cap Null(D) \cap Null(D^2) = \{0\}$ with $Null(\cdot)$ denotes the null space, the model (8) has a global minimizer.*

Proof. According to [40], we define the function

$$f(x,y) = \begin{cases} 1/r^2 & \text{if } \min(|x|, m-|x|) \le \frac{r-1}{2}, \min(|y|, n-|y|) \le \frac{r-1}{2},\\ 0 & \text{otherwise.}\end{cases}$$

From the definition of f, it is immediate to see that $f(x,y) = f(-x,-y)$. Thus, we can get that

$$\begin{aligned}\sum_{1\le i\le m,1\le j\le n} g_{i,j}^2 (H_r(|Du|))_{i,j} &= \sum_{1\le i\le m,1\le j\le n} g_{i,j}^2 \Big(\sum_{1\le s\le m,1\le t\le n} f(i-s,j-t)|Du|_{s,t}\Big)\\ &= \sum_{1\le s\le m,1\le t\le n} |Du|_{s,t} \Big(\sum_{1\le i\le m,1\le j\le n} f(s-i,t-j) g_{i,j}^2\Big)\\ &= \sum_{1\le s\le m,1\le t\le n} (H_r(g\circ g))_{s,t}|Du|_{s,t}\\ &= \sum_{1\le i\le m,1\le j\le n} (H_r(g\circ g))_{i,j}|Du|_{i,j}.\end{aligned} \tag{9}$$

And g is similar to g_1, g_2.

Then, the model (8) is equivalent to

$$\begin{aligned}\arg\min_{u,g_1,g_2} E(u,g_1,g_2) =& \frac{1}{2}\big(\langle \log(\gamma^2 + (Ku-f)^2), \mathbf{1}\rangle_X + \mu\|Ku-u_0\|_X^2\big) + \alpha\big(\|g_1 - \frac{M}{\alpha}\cdot\mathbf{1}\|_X^2 + \|g_2 - \frac{M}{\alpha}\cdot\mathbf{1}\|_X^2\big)\\ &+ \sum_{1\le i\le m,1\le j\le n} (H_r(g_1\circ g_1))_{i,j}|Du|_{i,j} + \sum_{1\le i\le m,1\le j\le n} (H_r(g_2\circ g_2))_{i,j}|D^2u|_{i,j}.\end{aligned} \tag{10}$$

Under the assumptions $\alpha > 0, M > 0$, due to $\gamma > 0$ and K is a linear operator, the model is bounded from below. And the function $E : X \times X \times X \to R$ is proper and continuous. According to the Weierstrass' theorem [52], it remains only to show the coercivity of $E(u,g_1,g_2)$, i.e., for every sequence $\{u^k, g_1^k, g_2^k\}$ such that $\|u^k\|_X + \|g_1^k\|_X + \|g_2^k\|_X \to \infty$, we

have $\lim_{k\to\infty} E(u^k, g_1^k, g_2^k) = \infty$. We prove it by contradiction. Suppose that there exists a subsequence of $\{u^k, g_1^k, g_2^k\}$ (also denoted as $\{u^k, g_1^k, g_2^k\}$) that $\{E(u^k, g_1^k, g_2^k)\}$ is bounded, we have that $\{\|Ku^k\|_X\}$, $\{\|Du^k\|_Y\}$, $\{\|D^2u^k\|_Z\}$, $\{\|g_1^k\|_X\}$, and $\{\|g_2^k\|_X\}$ are bounded. According to the assumption $Null(K) \cap Null(D) \cap Null(D^2) = \{0\}$, the sequence $\{u^k\}$ is a bounded sequence, which is a contradiction. Therefore, the existence of a global minimizer is deduced.

Assuming that (u^*, g_1^*, g_2^*) is a minimizer of (8), according to Theorem 3.1, then the following result is straightforward [53]:

$$u^* = \arg\min_u E(u, g_1^*, g_2^*), \qquad (g_1^*, g_2^*) = \arg\min_{g_1, g_2} E(u^*, g_1, g_2). \tag{11}$$

We remark that the adaptive model (8) is non-convex, therefore, it is difficult to find the global minimum in practice. However, one can still find its coordinate-wise minimums that satisfy (11).

According to (9) and (11), given u^*, the solutions of g_1 and g_2 are expressed as follows:

$$(g_1^*)_{i,j} = f(Du_{i,j}^*), \quad (g_2^*)_{i,j} = f(D^2u_{i,j}^*), \quad \text{and} \quad f(x) = \frac{M}{\alpha + (H_r(|x|))}. \tag{12}$$

Substituting g_1^* and g_2^* into (8), the solution of u can be obtained from the following optimization problem:

$$\begin{aligned}\arg\min_u \frac{1}{2}\big(\langle \log(\gamma^2 + (Ku - f)^2), \mathbf{1}\rangle_X + \mu\|Ku - u_0\|_X^2\big) + \alpha\big(\|g_1^* - \frac{M}{\alpha}\cdot\mathbf{1}\|_X^2 + \|g_2^* - \frac{M}{\alpha}\cdot\mathbf{1}\|_X^2\big)\\ + \sum_{1\le i\le m, 1\le j\le n} (g_1^*)_{i,j}^2 (H_r(|Du|))_{i,j} + \sum_{1\le i\le m, 1\le j\le n} (g_2^*)_{i,j}^2 (H_r(|D^2u|))_{i,j}.\end{aligned} \tag{13}$$

4. Numerical scheme and convergence analysis

Based on the analysis of the previous section, we adopt an alternating minimization scheme to decompose the model (8) into two strictly convex problems. It has the following two steps:

Step1: the u problem

$$\begin{aligned}\arg\min_u E(u, g_1^*, g_2^*) = \arg\min_u \frac{1}{2}\big(\langle \log(\gamma^2 + (Ku - f)^2), \mathbf{1}\rangle_X + \mu\|Ku - u_0\|_X^2\big)\\ + \sum_{1\le i\le m, 1\le j\le n} (H_r(g_1^* \circ g_1^*))_{i,j} |Du|_{i,j} + \sum_{1\le i\le m, 1\le j\le n} (H_r(g_2^* \circ g_2^*))_{i,j} |D^2u|_{i,j}.\end{aligned} \tag{14}$$

Step2: the (g_1, g_2) problem

$$\begin{aligned}\arg\min_{g_1, g_2} E(u^*, g_1, g_2) = \arg\min_{g_1, g_2} \alpha\big(\|g_1 - \frac{M}{\alpha}\cdot\mathbf{1}\|_X^2 + \|g_2 - \frac{M}{\alpha}\cdot\mathbf{1}\|_X^2\big)\\ + \sum_{1\le i\le m, 1\le j\le n} (g_1)_{i,j}^2 (H_r(|Du^*|))_{i,j} + \sum_{1\le i\le m, 1\le j\le n} (g_2)_{i,j}^2 (H_r(|D^2u^*|))_{i,j}.\end{aligned} \tag{15}$$

The algorithm for solving the proposed model (8) is summarized in **Algorithm** 2.

Algorithm 2: The alternating minimization method for solving (8).

Input: data f, parameters α, M, β, r.
Initialize: $g_1^0 = 0, g_2^0 = 0, \epsilon = 1e-5$ and $maxiter.out = 100$.
1: **While** $(\|u^{k+1} - u^k\|_F / \|u^k\|_F > \epsilon$ and $k \le maxiter.out)$ **Do**
2: Given g_1^k and g_2^k, update u^{k+1} by solving (14).
3: Given u^{k+1}, update g_1^{k+1} and g_2^{k+1} by solving (12).
4: **End while**(converged)
Output: The restored image u.

Since $E(u, g_1^*, g_2^*)$ is convex with respect to u, the u problem can be efficiently solved by ADMM. The main idea is to rewrite the unconstrained minimization problem (14) into a constrained one by introducing three auxiliary variables $p = Du$, $q = D^2u$, and $w = Ku$. The minimization of (14) is equivalent to the following constrained problem:

$$\begin{aligned}E(u, g_1^*, g_2^*) = \arg\min_{u,p,q,w} \frac{1}{2}\big(\langle \log(\gamma^2 + (w - f)^2), \mathbf{1}\rangle_X + \mu\|w - u_0\|_X^2\big)\\ + \sum_{1\le i\le m, 1\le j\le n} (H_r(g_1^* \circ g_1^*))_{i,j} |p|_{i,j} + \sum_{1\le i\le m, 1\le j\le n} (H_r(g_2^* \circ g_2^*))_{i,j} |q|_{i,j},\\ s.t. \qquad p = Du, q = D^2u, w = Ku.\end{aligned} \tag{16}$$

The corresponding augmented Lagrangian function of (16) is given by

$$\begin{aligned} L(u,p,q,w,\lambda_1,\lambda_2,\lambda_3) =& \frac{1}{2}\big(\langle \log(\gamma^2+(w-f)^2),\mathbf{1}\rangle_X + \mu\|w-u_0\|_X^2\big) + \sum_{1\le i\le m,1\le j\le n}(H_r(g_1^*\circ g_1^*))_{i,j}|p|_{i,j} \\ &+ \sum_{1\le i\le m,1\le j\le n}(H_r(g_2^*\circ g_2^*))_{i,j}|q|_{i,j} + \frac{\beta}{2}\big(\|p-Du+\frac{\lambda_1}{\beta}\|_Y^2 + \|q-D^2u+\frac{\lambda_2}{\beta}\|_Z^2 \\ &+ \|w-Ku+\frac{\lambda_3}{\beta}\|_X^2\big), \end{aligned} \tag{17}$$

where λ_1, λ_2, and λ_3 are the Lagrangian multipliers, β is a penalty parameter. ADMM minimizes the Lagrangian function with respect to the two variable groups u and (p, q, w). Since p, q, and w are decoupled with each other, they can be solved separately. Thus, (16) is decomposed into four simpler minimization subproblems.

(**a**) The u subproblem is

$$u^{k+1} = \arg\min_u \frac{\beta}{2}\big(\|p^k-Du+\frac{\lambda_1^k}{\beta}\|_Y^2 + \|q^k-D^2u+\frac{\lambda_2^k}{\beta}\|_Z^2 + \|w^k-Ku+\frac{\lambda_3^k}{\beta}\|_X^2\big). \tag{18}$$

By the optimal condition, we have

$$(D^*D+(D^2)^*D^2+K^*K)u^{k+1} = \frac{1}{\beta}(D^*(\beta p^k+\lambda_1^k)+(D^2)^*(\beta q^k+\lambda_2^k)+K^*(\beta w^k+\lambda_3^k)). \tag{19}$$

The periodic boundary condition is assumed, so K, D, and D^2 are block circulant with circulating block structure. The optimal u can be solved efficiently in the Fourier domain

$$u^{k+1} = \mathscr{F}^{-1}\left(\frac{\frac{1}{\beta}(\mathscr{F}(D^*(\beta p^k+\lambda_1^k)+(D^2)^*(\beta q^k+\lambda_2^k)+K^*(\beta w^k+\lambda_3^k)))}{\mathscr{F}(D^*D)+\mathscr{F}((D^2)^*D^2)+\mathscr{F}(K^*K)}\right), \tag{20}$$

where $\mathscr{F}$ denotes the discrete Fourier transform, $\mathscr{F}^{-1}$ is the inverse transform, and K^* is the conjugate operator of K.

(**b**) The p subproblem is

$$p^{k+1} = \arg\min_p \sum_{1\le i\le m,1\le j\le n}(H_r(g_1\circ g_1))_{i,j}|p|_{i,j} + \frac{\beta}{2}\|p-Du+\frac{\lambda_1}{\beta}\|_Y^2. \tag{21}$$

It can be solved by the shrinkage operator [54]

$$p_{i,j}^{k+1} = \max\{|Du^k-\frac{\lambda_1^k}{\beta}|_{i,j} - \frac{H_r(g_1^k\circ g_1^k)_{i,j}}{\beta}, 0\}\circ \mathrm{sign}((Du^k-(\lambda_1^k/\beta))_{i,j}), \tag{22}$$

where sign refers to 1 if the entry is greater than or equal to zero, and -1 if the entry is negative.

(**c**) The q subproblem is

$$q^{k+1} = \arg\min_q \sum_{1\le i\le m,1\le j\le n}(H_r(g_2\circ g_2))_{i,j}|q|_{i,j} + \frac{\beta}{2}\|q-D^2u+\frac{\lambda_2}{\beta}\|_Z^2. \tag{23}$$

Similarly, q can be solved by the two-dimensional shrinkage operator

$$q_{i,j}^{k+1} = \max\{|D^2u^k-\frac{\lambda_2^k}{\beta}|_{i,j} - \frac{H_r(g_2^k\circ g_2^k)_{i,j}}{\beta}, 0\}\circ \mathrm{sign}((D^2u^k-(\lambda_2^k/\beta))_{i,j}). \tag{24}$$

(**d**) The w subproblem is

$$w^{k+1} = \arg\min_w \frac{1}{2}\big(\langle \log(\gamma^2+(w-f)^2),\mathbf{1}\rangle_X + \mu\|w-u_0\|_X^2\big) + \frac{\beta}{2}\|w-Ku+\frac{\lambda_3}{\beta}\|_X^2. \tag{25}$$

Let

$$G(w) = \frac{1}{2}\big(\langle log(\gamma^2+(w-f)^2),\mathbf{1}\rangle_X + \mu\|w-u_0\|_X^2\big) + \frac{\beta}{2}\|w-Ku+\frac{\lambda_3}{\beta}\|_X^2, \tag{26}$$

then we obtain the solution by Newton's method

$$w^{k+1,l+1} = w^{k+1,l} - \frac{G'(w^{k,l+1})}{G''(w^{k,l+1})}, \tag{27}$$

where G' and G'' are the gradient and Hessian matrices of G, respectively. $w^{k+1,l+1}$ represents the result of the $(l+1)$-th Newton iteration in the $(k+1)$-th outer iteration.

(**e**) Finally, the multipliers λ_1, λ_2, and λ_3 are updated as follows:

$$\begin{aligned}\lambda_1^{k+1} &= \lambda_1^k + \beta(p^{k+1} - Du^{k+1}),\\ \lambda_2^{k+1} &= \lambda_2^k + \beta(q^{k+1} - D^2u^{k+1}),\\ \lambda_3^{k+1} &= \lambda_3^k + \beta(w^{k+1} - Ku^{k+1}).\end{aligned} \tag{28}$$

Therefore, the ADMM algorithm for solving the u problem is summarized in **Algorithm** 3.

Algorithm 3: The alternating direction method with multipliers for solving (14).

Input: data f, g_1^k, g_2^k, parameters β, r.
Initialize: $u = f, p, q, w, \lambda_1, \lambda_2, \lambda_3, \epsilon = 1e-5, maxiter.in = 10$.
1: **While** ($\|u^{k+1} - u^k\|_F / \|u^k\|_F > \epsilon$ and $k \le maxiter.in$) **Do**
2: Update u^{k+1} by (20).
3: Update (22), (24) for p^{k+1} and q^{k+1}, respectively.
4: Update w^{k+1} by (27).
5: Update λ_1^{k+1}, λ_2^{k+1} and λ_3^{k+1}, by (28), respectively.
6: **End Do**
Output: Restoring image u.

Next, we show that the sequence created by **Algorithm** 2 has a subsequence that converges to the coordinate-wise minimum point $(\hat{u}, \hat{g_1}, \hat{g_2})$ of the objective function E.

Coordinate-wise minimum point. Let $z \in \mathbb{R}^s$, we refer to each z_k, $k = 1, \ldots, N$, as a coordinate block of $z = (z_1, \ldots, z_N)$, where $z_k \in \mathbb{R}^{n_k}$ and $n_1 + \cdots + n_N = s$. We say that z is a coordinate-wise minimum point of f if $z \in domf$ and

$$f(z + (0, \ldots, d_k, \ldots, 0)) \ge f(z), \qquad d_k \in R^{n_k},$$

where $(0, \ldots, d_k, \ldots, 0)$ is a vector in $R^{n_1+\cdots+n_N}$ whose k-th coordinate block is d_k and whose other coordinates are zero.

Theorem 4.1. *Let (u^k, g_1^k, g_2^k) be the sequence derived from Algorithm* 2. *Then (u^k, g_1^k, g_2^k) converges to a coordinate-wise minimum $(\hat{u}, \hat{g_1}, \hat{g_2}) \in X \times X \times X$ (up to a subsequence), i.e., for any $(u, g_1, g_2) \in X \times X \times X$, one has*

$$E(\hat{u}, \hat{g_1}, \hat{g_2}) \le E(u, \hat{g_1}, \hat{g_2}) \quad \text{and} \quad E(\hat{u}, \hat{g_1}, \hat{g_2}) \le E(\hat{u}, g_1, g_2). \tag{29}$$

Proof. First, we observe the following inequality from Algorithm 2:

$$E(u^{k+1}, g_1^{k+1}, g_2^{k+1}) \le E(u^{k+1}, g_1^k, g_2^k) \le E(u^k, g_1^k, g_2^k),$$

which implies that the sequence $E(u^k, g_1^k, g_2^k)$ is bounded and decreases in each iteration. Since (8) is coercive, the boundedness of $E(u^k, g_1^k, g_2^k)$ suggests that (u^k, g_1^k, g_2^k) is bounded. Then we can find a subsequence $\{(u^{n_k}, g_1^{n_k}, g_2^{n_k})\} \subset \{(u^k, g_1^k, g_2^k)\}$ and $(\hat{u}, \hat{g_1}, \hat{g_2}) \in X \times X \times X$, such that they satisfy

$$(u^{n_k}, g_1^{n_k}, g_2^{n_k}) \to (\hat{u}, \hat{g_1}, \hat{g_2}).$$

On the other hand, we show that $(\hat{u}, \hat{g_1}, \hat{g_2})$ is a coordinate-wise minimum. In fact, for any $(u, g_1, g_2) \in X \times X \times X$, we have

$$\begin{aligned}E(u^{n_{k+1}}, g_1^{n_{k+1}}, g_2^{n_{k+1}}) &\le E(u^{n_k+1}, g_1^{n_k+1}, g_2^{n_k+1})\\ &\le E(u^{n_k+1}, g_1^{n_k}, g_2^{n_k})\\ &\le E(u, g_1^{n_k}, g_2^{n_k})\end{aligned}$$

and

$$E(u^{n_k}, g_1^{n_k}, g_2^{n_k}) \le E(u^{n_k}, g_1, g_2)$$

Since the objective function is continuous, letting $k \to \infty$, we deduce that

$$E(\hat{u}, \hat{g_1}, \hat{g_2}) \le E(u, \hat{g_1}, \hat{g_2})$$

and

$$E(\hat{u}, \hat{g_1}, \hat{g_2}) \le E(\hat{u}, g_1, g_2).$$

The proof is completed.

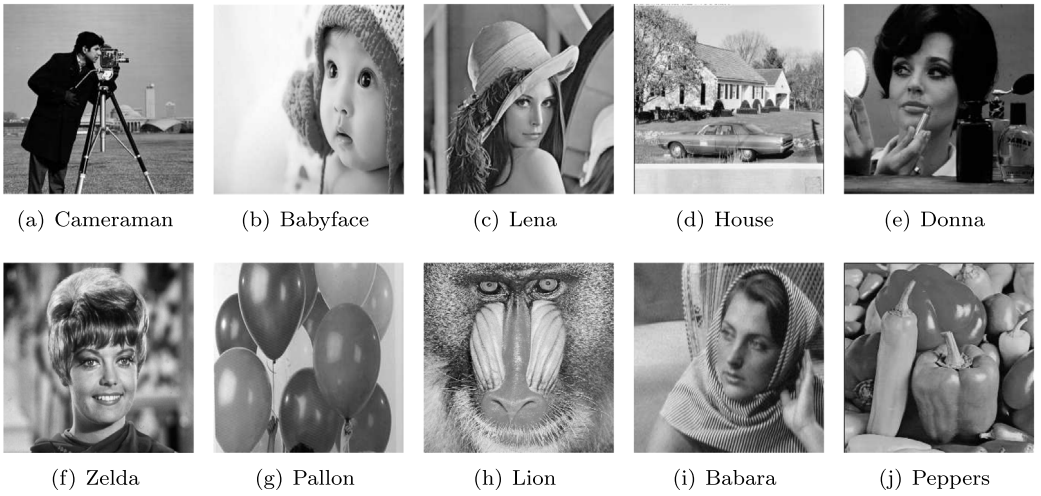

(a) Cameraman (b) Babyface (c) Lena (d) House (e) Donna

(f) Zelda (g) Pallon (h) Lion (i) Babara (j) Peppers

Fig. 1. The original images.

5. Experiments and discussions

This section is divided into five parts. Section 5.1 gives experimental settings. Section 5.2 discusses the choice of parameters in the proposed method. Sections 5.3 and 5.4 show denoising and deblurring cases. Section 5.5 presents detailed discussion to demonstrate the validity and superiority of the proposed model. Section 5.6 numerically demonstrates the convergence of the proposed algorithm.

5.1. Experiment setting

Fig. 1 shows ten gray-scale test images. For simplicity, the pixel values of images are normalized to $[0, 1]$. In all experiments, we generate the noisy image f by using the following degradation:

$$f = Ku + v = Ku + \varepsilon\frac{\eta_1}{\eta_2}, \tag{30}$$

where $\varepsilon > 0$ represents the noise level and η_1 and η_2 are independent random variables following Gaussian distribution with mean 0 and variance 1.

We use the peak signal to noise ratio (PSNR) [55,56] and the structural similarity index (SSIM) [57] to quantitatively measure the image quality. They are defined as follows:

$$\text{PSNR} = 10\log_{10}\frac{N(Max_u)^2}{\|u-u^*\|_F^2},$$

$$\text{SSIM} = \frac{(2\mu_u\mu_{u^*})(2\sigma_{uu^*}+c_2)}{(\mu_u^2+\mu_{u^*}^2+c_1)(\sigma_u^2+\sigma_{u^*}^2+c_2)},$$

where u^* is the ground truth, u is the recovered image, N is the size of images, Max_u is the maximum pixel of image, μ_u and μ_{u^*} are the mean values of images u and u^*, σ_u and σ_{u^*} are the standard variance of image u and u_*, respectively, σ_{uu^*} is the covariance of u and u^*, and $c_1, c_2 > 0$ are constants. Generally speaking, high PSNR and SSIM values imply better image quality.

We compare the proposed method (8) (termed as HTVAM) with the total variation convex model (termed as TVCM) [18] and the median filter (termed as MED). For a fair comparison, we adjust the parameters of HTVAM and TVCM in experiments to obtain the best PSNR results under the condition $8\mu\gamma^2 = 1$.

In the proposed method, the stopping condition is

$$\frac{\|u^{k+1}-u^k\|_F}{\|u^k\|_F} \le 1\times 10^{-5}. \tag{31}$$

All the experiments are performed under Windows 10 and MATLAB 2012a running on an ASUS laptop with an AMD E2-6110 CPU with AMD Radeon R2 Graphics with 1.50 GHz and 4 GB of RAM.

Table 1
The PSNR (dB), SSIM, and time (in s) with respect to the different number of inner iterations.

	Iteration	5	10	20	50	100	200
Cameraman	PSNR	27.51	29.12	28.69	28.23	28.10	28.08
	SSIM	0.8498	0.8702	0.8527	0.8360	0.8309	0.8304
	Time	11.35	18.86	34.85	84.04	164.51	220.64
Pallon	PSNR	32.00	34.72	34.64	34.43	34.39	34.39
	SSIM	0.9006	0.9173	0.9163	0.9148	0.9146	0.9146
	Time	9.53	15.80	27.57	63.79	95.02	106.33

Table 2
The PSNR (dB), SSIM, and time (in s) with respect to the different number of Newton iterations.

	Iteration	1	10	20	30	40	50	100
Babyface	PSNR	34.64	34.83	34.83	34.83	34.83	34.83	34.83
	SSIM	0.9481	0.9514	0.9514	0.9514	0.9514	0.9514	0.9514
	Time	23.20	26.62	26.92	27.69	28.62	27.81	32.14
Cameraman	PSNR	27.83	29.12	29.13	29.13	29.13	29.13	29.13
	SSIM	0.8157	0.8702	0.8705	0.8704	0.8705	0.8704	0.8705
	Time	13.44	18.85	23.43	28.86	34.03	37.05	64.30

5.2. Parameter discussion

In this subsection, we focus on the choices of the parameters α, M, r, β, the number of inner iterations *maxiter.in*, and the number of Newton iterations *maxiter.newton*. For simplicity, we just discuss denoising cases with $\varepsilon = 0.02$.

(1) Parameters: *maxiter.in* and *maxiter.newton*. In order to study the sensitivity of the number of inner iterations for solving the u problem, we use the image Cameraman ($\alpha = 0.15, M = 0.12, r = 45, \beta = 15$) and Pallon ($\alpha = 0.11, M = 0.1, r = 15, \beta = 16$) as examples and set the number of Newton iterations $maxiter.newton = 10$. The test results are displayed in Table 1. From Table 1, we get that the number of inner iterations $maxiter.in = 10$ is best for all tests in terms of PSNR, SSIM, and CPU time.

Next, we discuss the selection of the number of Newton iterations *maxiter.newton* in Algorithm 3. Our experiments are tested on Babyface ($\alpha = 0.14, M = 0.12, r = 39, \beta = 16$) and Cameraman ($\alpha = 0.15, M = 0.12, r = 45, \beta = 15$) with $maxiter.in = 10$. Table 2 illustrates that the PSNR and SSIM values are stable with respect to $maxiter.newton \geq 10$. However, the overall computational time increases as the iteration number increases. So we choose $maxiter.newton = 10$ for all experiments. It is worth noting that the above observations are also generally true for other test images.

(2) Parameters: α, M, r, and β. We study the impact of parameters α, M, r, and β in Fig. 2. We test on three images: Babyface, Donna, and Pallon corrupted by Cauchy noise with the noise level $\varepsilon = 0.02$. Fig. 2(a) and (d) indicate that the PSNR and SSIM values can obtain the highest with α in 0.12 nearby. Since our experiments involve various data and different noise levels, we empirically set the optimal range of α to [0.10, 0.20] with increment of 0.01. Similarly, we empirically set M from [0.01, 0.20] with increment of 0.01.

For the window size of the median filter r, the PSNR and SSIM perform obvious improvement when r is increased from 0 to 10. Moreover, we also observe that PSNR and SSIM curves are stable when r further goes increasing, see Fig. 2(c) and (f). Due to the diversity of experiments, we choose $r \in [3, 55]$ with increment of 2 in all experiments. Similarly, we empirically set β from [8, 25] with increment of 1.

5.3. Image denoising

Figs. 3 and 4 show the denoising results at different noise levels ($\varepsilon = 0.02$ and $\varepsilon = 0.04$) for the testing images, respectively. The restored images of MED show residual noise and oversmoothed image edges. Although the noise is well removed by TVCM, some artifacts are introduced in the flat ramp regions. As a comparison, the proposed HTVAM obtains the best performance in terms of noise removal and detail preservation. The quantitative results in Tables 3 and 4 show that HTVAM gets the highest PSNR and SSIM values, which are consistent with the visual comparison.

Fig. 5 shows the zoomed-in regions of the recovered images. Compared with MED and TVCM, the proposed method not only preserves details and textures clearly in the ramp regions, but also gets good recovery in the homogeneous regions.

5.4. Image deblurring

Fig. 6 shows the restored images for deblurring and denoising. We test the 9×9 Gaussian blur with standard deviation 1. The blurring images are generated by using the MATLAB function "imfilter" with periodic boundary condition. Then the blurry images are corrupted by Cauchy noise with $\varepsilon = 0.02$. We can observe that the restored results of MED lose many image details. TVCM generates typical staircase effects, see Fig. 6(o). In comparison, our results exhibit more details with fewer artifacts. Table 5 shows the PSNR and SSIM values of the deblurring and denoising experiments, which are quite competitive with other compared methods.

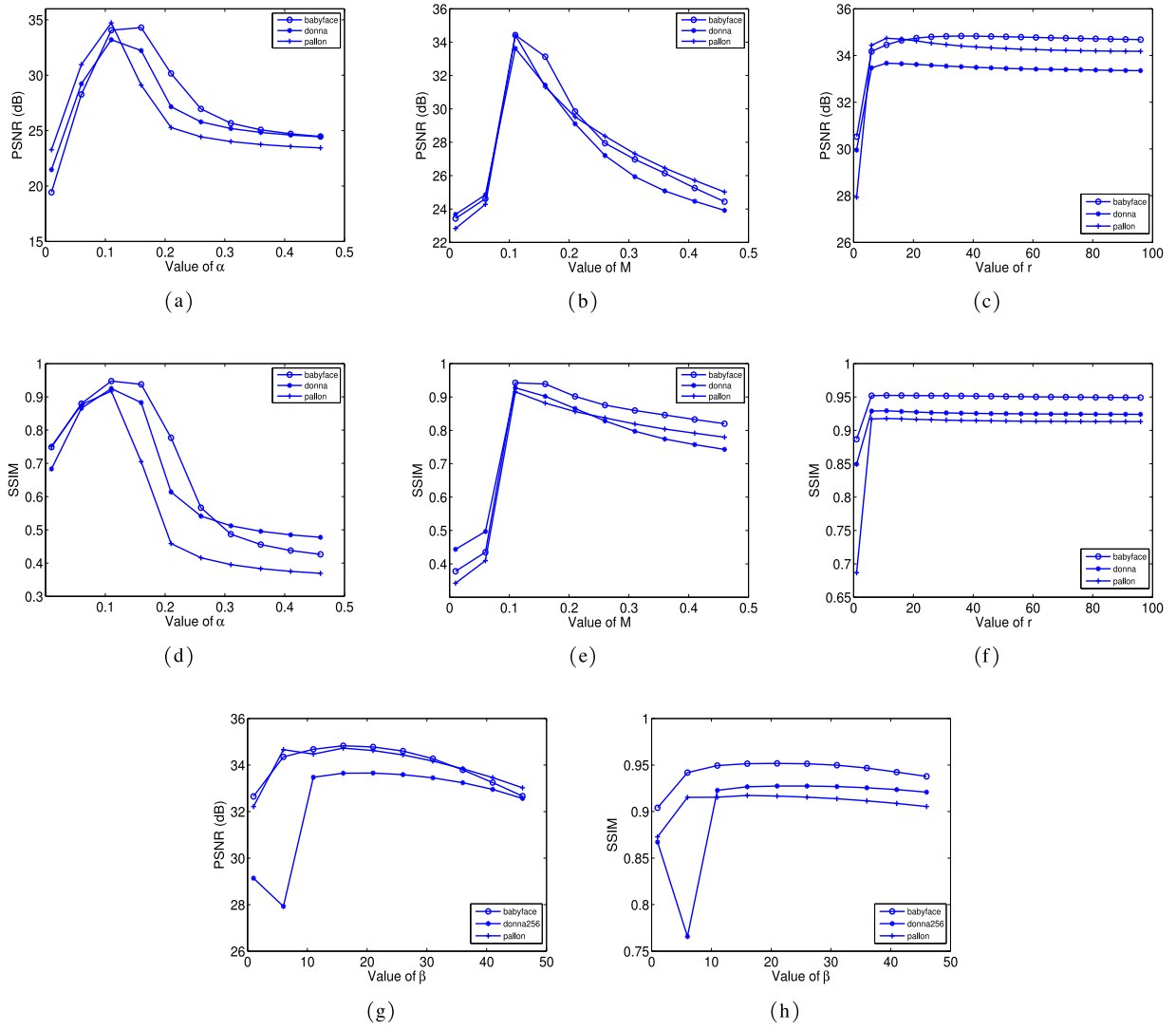

Fig. 2. Top row: the PSNR value with respect to α, M, and r. Middle row: the SSIM value with respect to α, M, and r. Bottom row: the PSNR and SSIM values with respect to β.

Table 3
The PSNR and SSIM values of noisy images and recovered images of different methods at $\varepsilon = 0.02$.

Images	Noisy		MED		TVCM		HTVAM	
	PSNR	SSIM	PSNR	SSIM	PSNR	SSIM	PSNR	SSIM
Cameraman	19.14	0.3550	26.19	0.7950	28.37	0.8290	**29.12**	**0.8702**
Babyface	19.12	0.2586	31.98	0.8805	33.45	0.9277	**34.83**	**0.9514**
Lena	19.12	0.3661	29.61	0.8607	30.86	0.8813	**31.72**	**0.9055**
House	19.11	0.4469	25.28	0.7484	27.86	0.8262	**28.13**	**0.8578**
Donna	19.25	0.3070	31.55	0.8692	32.76	0.9049	**33.62**	**0.9275**
Zelda	19.12	0.5352	33.54	0.9444	34.61	0.9546	**35.40**	**0.9626**
Pallon	19.16	0.2312	31.79	0.8541	33.84	0.8950	**34.72**	**0.9173**
Lion	19.19	0.5797	20.59	0.5020	24.51	0.7646	**24.73**	**0.7745**
Babara	19.15	0.4759	22.88	0.7304	26.59	0.8172	**27.63**	**0.8606**
Peppers	19.16	0.3635	29.52	0.8533	30.95	0.8862	**31.41**	**0.8993**

5.5. Detailed discussion

In this subsection, we discuss the rationality and superiority of selecting regularization parameters (g_1 and g_2) adaptively. Taking degraded Cameraman and Lion images ($\varepsilon = 0.02$) as examples, Fig. 7 presents the original images, the restored

(a) Noisy image: 19.14 (b) MED: 26.19 (c) TVCM: 28.37 (d) HTVAM: 29.12

(e) Noisy image: 19.12 (f) MED: 31.98 (g) TVCM: 33.45 (h) HTVAM: 34.83

(i) Noisy image: 19.16 (j) MED: 31.79 (k) TVCM: 33.84 (l) HTVAM: 34.72

(m) Noisy image: 19.19 (n) MED: 20.59 (o) TVCM: 24.51 (p) HTVAM: 24.73

(q) Noisy image: 19.15 (r) MED: 22.88 (s) TVCM: 26.59 (t) HTVAM: 27.63

Fig. 3. Denoising results of three methods at $\varepsilon = 0.02$ (each value in parentheses represents the corresponding PSNR (dB) value of the restored image). From left to right: the noisy images, MED, TVCM, and HTVAM.

(a) Noisy image: 16.23 (b) MED: 24.83 (c) TVCM: 26.66 (d) HTVAM: 27.32

(e) Noisy image: 16.24 (f) MED: 28.83 (g) TVCM: 31.13 (h) HTVAM: 32.22

(i) Noisy image: 16.23 (j) MED: 27.34 (k) TVCM: 28.63 (l) HTVAM: 29.33

(m) Noisy image: 16.25 (n) MED: 24.18 (o) TVCM: 25.82 (p) HTVAM: 26.08

(q) Noisy image: 16.30 (r) MED: 28.68 (s) TVCM: 30.44 (t) HTVAM: 31.14

Fig. 4. Denoising results of three methods at $\varepsilon = 0.04$ (each value in parentheses represents the corresponding PSNR (dB) value of the restored image). From left to right: the noisy images, MED, TVCM, and HTVAM.

(a) Original image (b) MED (c) TVCM (d) HTVAM

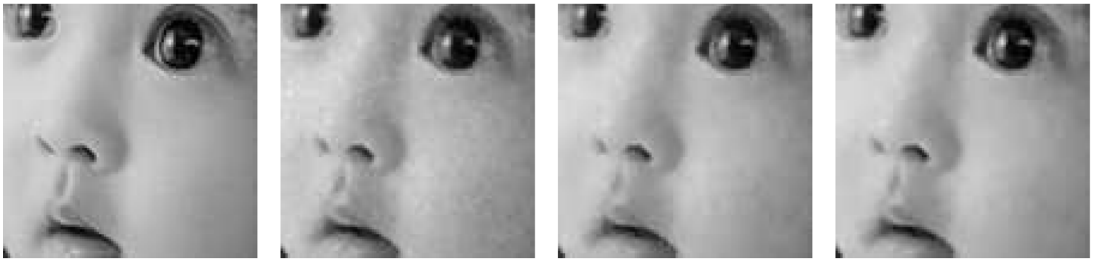

(e) Original image (f) MED (g) TVCM (h) HTVAM

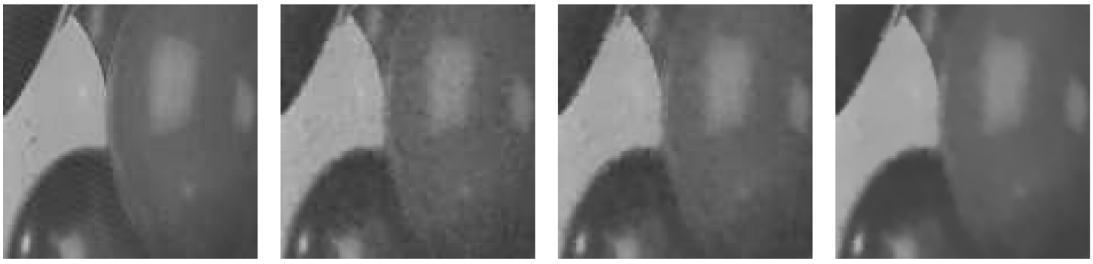

(i) Original image (j) MED (k) TVCM (l) HTVAM

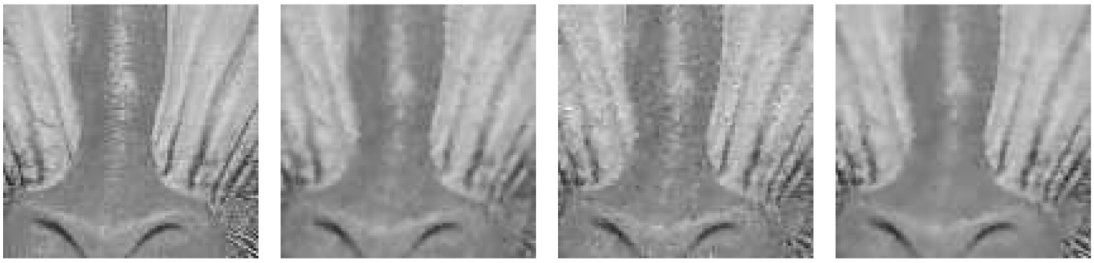

(m) Original image (n) MED (o) TVCM (p) HTVAM

(q) Original image (r) MED (s) TVCM (t) HTVAM

Fig. 5. The zoomed-in regions of the restored images in Fig. 3. From left to right: the original images, MED, TVCM, and HTVAM.

(a) Blurred image: 18.28 (b) MED: 24.42 (c) TVCM: 26.21 (d) HTVAM: 26.51

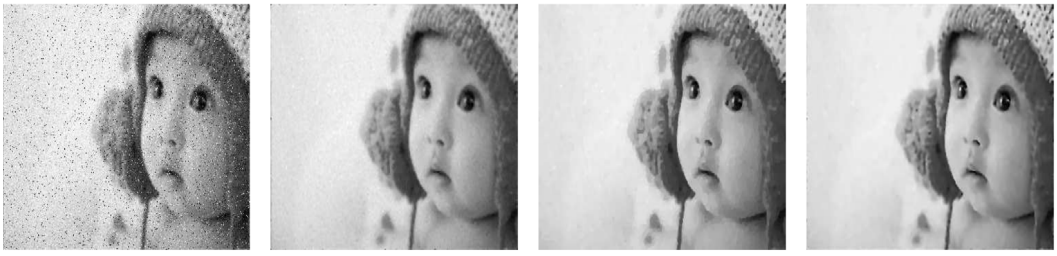

(e) Blurred image: 18.91 (f) MED: 29.98 (g) TVCM: 31.97 (h) HTVAM: 32.66

(i) Blurred image: 18.72 (j) MED: 27.31 (k) TVCM: 28.81 (l) HTVAM: 29.04

(m) Blurred image: 18.18 (n) MED: 23.99 (o) TVCM: 25.13 (p) HTVAM: 25.26

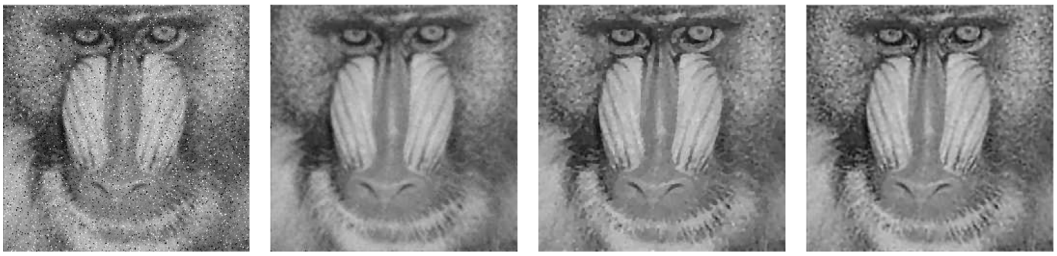

(q) Blurred image: 17.29 (r) MED: 20.90 (s) TVCM: 21.15 (t) HTVAM: 21.26

Fig. 6. Restoration results of different methods for blurred images with Cauchy noise at $\varepsilon = 0.02$ (each value in parentheses represents the corresponding PSNR (dB) value of the restored image). From left to right: the blurred images with Cauchy noise, MED, TVCM, and HTVAM.

Table 4
The PSNR and SSIM values of noisy images and recovered images of different methods at $\varepsilon = 0.04$.

Images	Noisy		MED		TVCM		HTVAM	
	PSNR	SSIM	PSNR	SSIM	PSNR	SSIM	PSNR	SSIM
Cameraman	16.23	0.2442	24.83	0.6706	26.66	0.7812	**27.32**	**0.8192**
Babyface	16.24	0.1516	28.83	0.7261	31.13	0.8853	**32.22**	**0.9252**
Lena	16.23	0.2444	27.34	0.7483	28.63	0.8308	**29.33**	**0.8636**
House	16.25	0.3144	24.18	0.6590	25.82	0.7492	**26.08**	**0.7957**
Donna	16.30	0.1887	28.68	0.7362	30.44	0.8638	**31.14**	**0.8860**
Zelda	16.22	0.3884	30.04	0.8587	32.65	0.9249	**33.24**	**0.9362**
Pallon	16.26	0.1318	28.74	0.7055	31.74	0.8698	**32.55**	**0.8932**
Lion	16.28	0.4241	20.16	0.4600	22.56	0.6486	**22.63**	**0.6560**
Babara	16.27	0.3422	22.11	0.6483	24.46	0.7341	**24.92**	**0.7937**
Peppers	16.26	0.2392	27.26	0.7472	28.71	0.8369	**29.05**	**0.8635**

Table 5
The PSNR and SSIM values of the images degraded by Gaussian blur and Cauchy noise and recovered images of different methods at $\varepsilon = 0.02$.

Images	Blurred		MED		TVCM		HTVAM	
	PSNR	SSIM	PSNR	SSIM	PSNR	SSIM	PSNR	SSIM
Cameraman	18.28	0.2639	24.41	0.7480	26.21	0.8021	**26.51**	**0.8215**
Babyface	18.91	0.2310	29.98	0.8551	31.97	0.9102	**32.66**	**0.9314**
Lena	18.71	0.3008	27.31	0.8061	28.81	0.8414	**29.04**	**0.8597**
House	18.18	0.3117	23.99	0.6973	25.13	0.7414	**25.27**	**0.7560**
Donna	19.02	0.2670	29.60	0.8385	31.14	0.8893	**31.65**	**0.9032**
Zelda	19.02	0.5179	32.56	0.9355	33.35	0.9428	**34.00**	**0.9527**
Pallon	19.00	0.1991	30.58	0.8309	32.34	0.8826	**32.69**	**0.8975**
lion	17.29	0.2669	20.90	0.4611	21.15	0.4998	**21.26**	**0.5217**

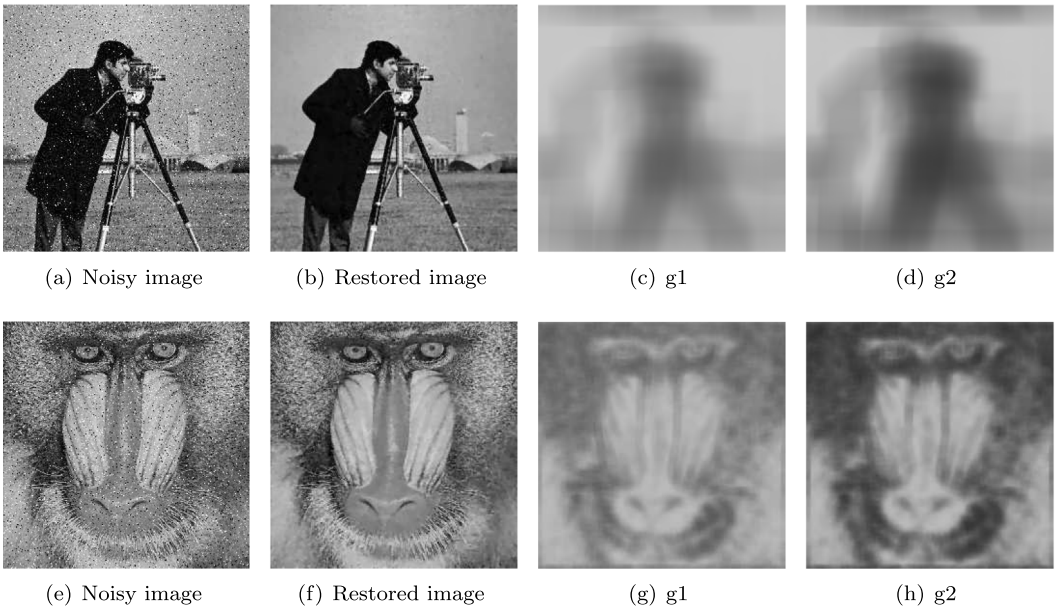

Fig. 7. Numerical behaviors of g_1 and g_2 at $\varepsilon = 0.02$. From left to right: the noisy image, the restored image, the final g_1 and g_2. This figure shows the rationality of regularization parameters.

images, and final spatially varying regularization parameters g_1 and g_2. It can be observed that the values of regularization parameters are small in details and texture regions, and are large in homogeneous regions, as shown in (c), (d), (g), and (h). Therefore, it demonstrates the rationality of adaptive selection of regularization parameters.

Next, we study the superiority of the proposed HTVAM. Fig. 8 presents the restored images of TV adaptive model (adaptive adjusting parameter α in (3), termed as TVAM), TV and high-order TV model (6) (termed as HTVM), and HTVAM. The Cameraman, Babyface, and Lion images are degraded by Cauchy noise with $\varepsilon = 0.02$. We can observe that the restored images of HTVAM are sufficiently denoised in homogeneous regions while keeping more details. In contrast, TVAM produces staircase artifacts in smooth regions, such as the background of (b) and the face of (f). Comparing HTVM and HTVAM, it can

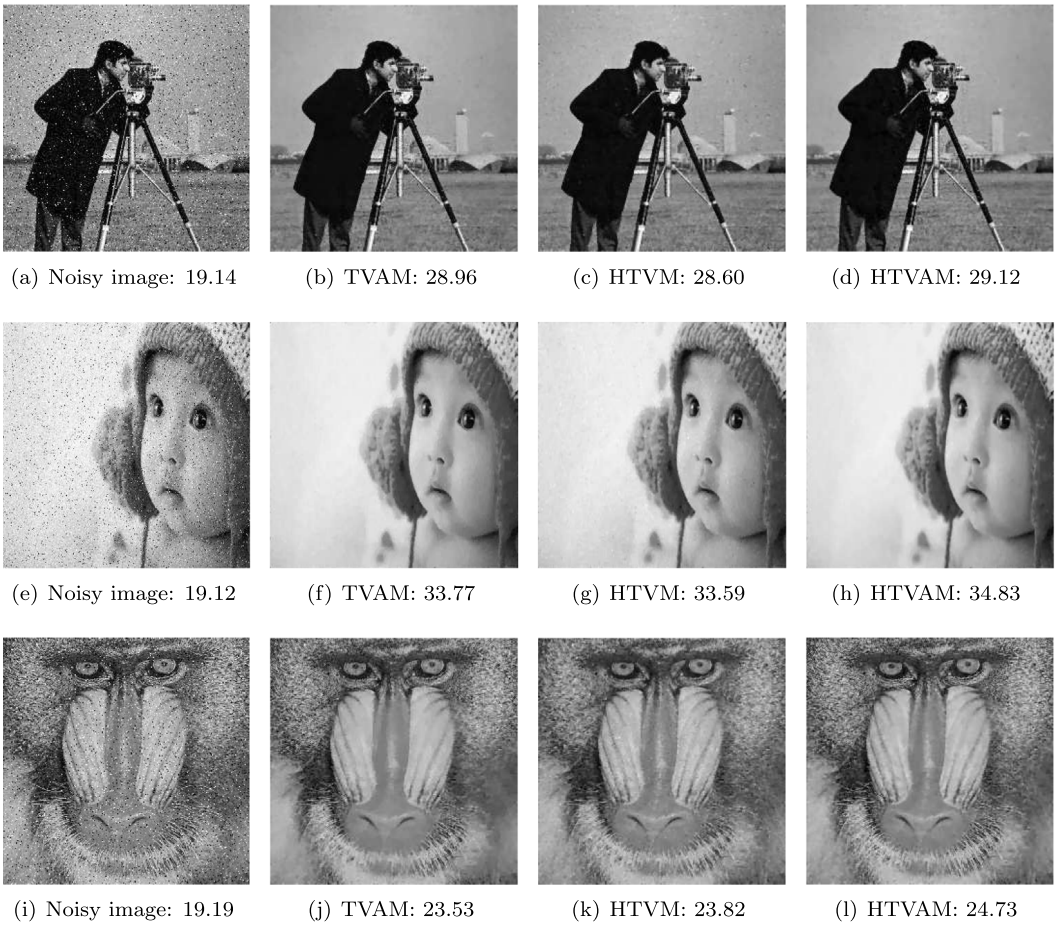

(a) Noisy image: 19.14 (b) TVAM: 28.96 (c) HTVM: 28.60 (d) HTVAM: 29.12

(e) Noisy image: 19.12 (f) TVAM: 33.77 (g) HTVM: 33.59 (h) HTVAM: 34.83

(i) Noisy image: 19.19 (j) TVAM: 23.53 (k) HTVM: 23.82 (l) HTVAM: 24.73

Fig. 8. Denoising results at $\varepsilon = 0.02$ (each value in parentheses represents the corresponding PSNR (dB) value of the restored image). From left to right: the noisy images, TVAM, HTVM, and HTVAM. This figure shows the superiority of the proposed model.

Table 6
The PSNR and SSIM values of noisy images and recovered images of TVAM, HTVM, and HTVAM ($\varepsilon = 0.02$)

Images	Noisy		TVAM		HTVM		HTVAM	
	PSNR	SSIM	PSNR	SSIM	PSNR	SSIM	PSNR	SSIM
Cameraman	19.14	0.3550	28.96	0.8677	28.60	0.8349	**29.12**	**0.8702**
Babyface	19.12	0.2586	33.77	0.9241	33.59	0.9095	**34.83**	**0.9514**
Lion	19.19	0.5797	23.53	0.7287	23.82	0.7420	**24.73**	**0.7745**

be seen that HTVAM produces smoother homogeneous regions with more preserved textures than HTVM, which can be seen in the background of (d) and the nose of (l). The corresponding PSNR and SSIM values are listed in Table 6.

5.6. Convergence analysis

In Theorem 4.1, we have proved that the sequence of the proposed algorithm has a subsequence that converges to the coordinate-wise minimum point. To numerically illustrate the convergence of the proposed algorithm, we test three images, Lena degraded by Cauchy noise with $\varepsilon = 0.02$; Pallon degraded by Cauchy noise with $\varepsilon = 0.04$; Lion blurred by Gaussian blur kernel with size 9 and standard deviation 1 and corrupted by Cauchy noise with $\varepsilon = 0.02$. Fig. 9 shows the relative error curves of the successive restored image u ($\|u^{k+1} - u^k\|_F / \|u^k\|_F$). We can observe that the relative error keeps decreasing as the iteration number increases, which numerically illustrates the convergence of our algorithm.

6. Conclusion

In this paper, a new model is proposed by a combination of TV and high-order TV for Cauchy noise removal. The proposed model can adaptively estimate the weights of TV and high-order TV from the restored image. Thus, it can preserve sharp

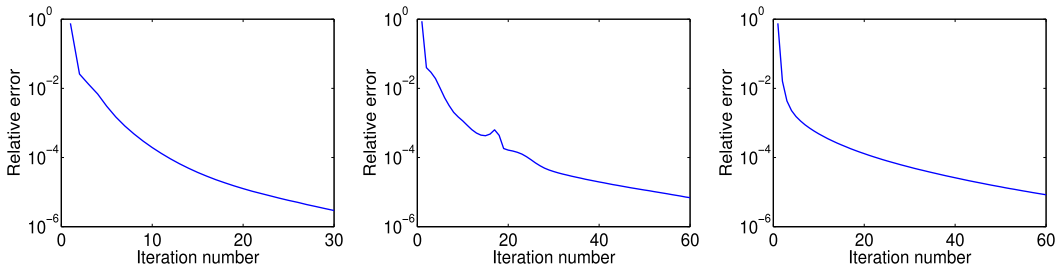

(a) Lena (b) Pallon (c) Lion

Fig. 9. Curves of relative error values versus iterations.

edges while maintaining the smoothness in flat areas. An efficient alternating minimization scheme is presented for solving the proposed model. In addition, we discuss the existence of the numerical solution and the convergence of the proposed algorithm. Extensive numerical experiments demonstrate the superiority of the proposed method in terms of visual quality and quantitative indexes.

Acknowledgments

This research is supported by NSFC, China (No. 61876203 and 61772003), the Fundamental Research Funds for the Central Universities, China (No. ZYGX2016J132), Science Strength Promotion Programme of UESTC, China, National Postdoctoral Program for Innovative Talents (No. BX20180252), and Fuyang Municipal Government-Fuyang Normal University Horizontal Cooperation, China Projects (No. XDHX201727).

References

[1] L.I. Rudin, S. Osher, E. Fatemi, Nonlinear total variation based noise removal algorithms, Physica D 60 (1) (1992) 259–268.
[2] G. Aubert, P. Kornprobst, Mathematical Problems in Image Processing: Partial Differential Equations and the Calculus of Variations, Springer Publishing Company, Incorporated, 2010.
[3] Bovik, C. Alan, Handbook of Image and Video Processing, second ed., Publishing House of Electronics Industry, 2006.
[4] L.J. Deng, T.Z. Huang, X.L. Zhao, T.X. Jiang, A directional global sparse model for single image rain removal, Appl. Math. Model. 59 (2018) 662–679.
[5] J. Huang, M. Donatelli, R.H. Chan, nonstationary iterated thresholding algorithms for image deblurring, Inverse Probl. Imag. 7 (3) (2013) 717–736.
[6] X.L. Zhao, T.Z. Huang, X.G. Lv, Z.B. Xu, J. Huang, Kronecker product approximations for image restoration with new mean boundary conditions, Appl. Math. Model. 36 (1) (2012) 225–237.
[7] T.H. Ma, Y. Lou, T.Z. Huang, Truncated ℓ_{1-2} models for sparse recovery and rank minimization, SIAM J. Imag. Sci. 10 (3) (2017) 1346–1380.
[8] N. Krishnan, S. Muthukumar, S. Ravi, D. Shashikala, P. Pasupathi, Image Restoration by Using Evolutionary Technique to Denoise Gaussian and Impulse Noise, Springer International Publishing, 2013.
[9] F. Luisier, T. Blu, M. Unser, Image denoising in mixed Poisson Gaussian noise, IEEE Trans. Image Process. 20 (3) (2011) 696–708.
[10] T.A. Nguyen, W.S. Song, M.C. Hong, Spatially adaptive denoising algorithm for a single image corrupted by Gaussian noise, IEEE T. Consum. Electr. 56 (3) (2010) 1610–1615.
[11] Y.Q. Dong, T.Y. Zeng, A convex variational model for restoring blurred images with multiplicative noise, SIAM J. Imaging Sci. 6 (3) (2013) 1598–1625.
[12] X.L. Zhao, F. Wang, M.K. Ng, A new convex optimization model for multiplicative noise and blur removal, SIAM J. Imaging Sci. 7 (1) (2014) 456–475.
[13] A. Ullah, W. Chen, M.A. Khan, A new variational approach for restoring images with multiplicative noise, Comput. Math. Appl. 71 (10) (2016) 2034–2050.
[14] R.H. Chan, Y.Q. Dong, M. Hintermüller, An efficient two-phase L1-TV method for restoring blurred images with impulse noise, IEEE Trans. Image Process. 19 (7) (2010) 1731–1739.
[15] M. Nikolova, A variational approach to remove outliers and impulse noise, J. Math. Imaging Vision 20 (1) (2004) 99–120.
[16] P.N. John, Numerical calculation of stable densities and distribution functions, Comm. Statist. Stoch. Models 13 (4) (1997) 759–774.
[17] J. Nolan, Stable Distributions: Models for Heavy-Tailed Data, Birkhauser Boston, 2003.
[18] F. Sciacchitano, Y.Q. Dong, T.Y. Zeng, Variational approach for restoring blurred images with Cauchy noise, SIAM J. Imaging Sci. 8 (3) (2015) 1894–1922.
[19] A. Achim, E.E. Kuruoglu, Image denoising using bivariate α-stable distributions in the complex wavelet domain, Signal Proc. Let. 12 (1) (2005) 17–20.
[20] Y.C. Chang, S.R. Kadaba, P.C. Doerschuk, S.B. Gelfand, Image restoration using recursive Markov random field models driven by Cauchy distributed noise, IEEE Signal Process. Lett. 8 (3) (2001) 65–66.
[21] T. Wan, N. Canagarajah, A. Achim, Segmentation of noisy colour images using Cauchy distribution in the complex wavelet domain, IET Image Process. 5 (2) (2011) 159–170.
[22] Z.M. Jin, X.Q. Yang, A variational model to remove the multiplicative noise in ultrasound images, J. Math. Imaging Vision 39 (1) (2011) 62–74.
[23] X.L. Zhao, W. Wang, T.Y. Zeng, T.Z. Huang, M.K. Ng, Total variation structured total least squares method for image restoration, SIAM J. Sci. Comput. 35 (6) (2013) 1304–1320.
[24] A. Bovik, Handbook of image and video processing, Acad. Press 62 (10) (2000) 4632–4636.
[25] J.J. Mei, Y.Q. Dong, T.Z. Huang, W.T. Yin, Cauchy noise removal by nonconvex ADMM with convergence guarantees, J. Sci. Comput. (2017) 1–24, http://dx.doi.org/10.1007/s10915--017--0460--5.
[26] P.F. Liu, L. Xiao, Efficient multiplicative noise removal method using isotropci second order total variation, Comput. Math. Appl. 70 (8) (2015) 2029–2048.
[27] G. Liu, T.Z. Huang, J. Liu, High-order TVL1-based images restoration and spatially adapted regularization parameter selection, Comput. Math. Appl. 67 (10) (2014) 2015–2026.
[28] X. Zhang, W. Ye, An adaptive fourth-order partial differential equation for image denoising, Comput. Math. Appl. 74 (10) (2017) 2529–2545.

[29] S. Wang, T.Z. Huang, X.L. Zhao, J.J. Mei, J. Huang, Speckle noise removal in ultrasound images by first- and second-order total variation, Numer. Algorithms 78 (2) (2018) 513–533.
[30] F. Li, C. Shen, J.S. Fan, C.L. Shen, Image restoration combining a total variational filter and a fourth-order filter, J. Vis. Commun. Image Represent. 18 (4) (2007) 322–330.
[31] A. Chambolle, P.L. Lions, Image recovery via total variation minimization and related problems, Numer. Math. 76 (2) (1997) 167–188.
[32] M. Lysaker, A. Lundervold, X.C. Tai, Noise removal using fourth-order partial differential equation with applications to medical magnetic resonance images in space and time, IEEE Trans. Image Process. 12 (12) (2003) 1579–1590.
[33] Y.L. You, M. Kaveh, Fourth-order partial differential equations for noise removal, IEEE Trans. Image Process. 9 (10) (2000) 1723–1730.
[34] S. Setzer, G. Steidl, Variational methods with higher order derivatives in image processing, Approx. 12 (2008) 360–386.
[35] S. Lefkimmiatis, A. Bourquard, M. Unser, Hessian-based norm regularization for image restoration with biomedical applications, IEEE Trans. Image Process. 21 (3) (2012) 983–995.
[36] K. Bredies, K. Kunisch, T. Pock, Total generalized variation, SIAM J. Imaging Sci. 3 (3) (2010) 492–526.
[37] J.J. Mei, T.Z. Huang, Primal–dual splitting method for high-order model with application to image restoration, Appl. Math. Model. 40 (3) (2015) 2322–2332.
[38] M. Bertalmio, V. Caselles, B. Rougé, A. Solé, TV based image restoration with local constraints, J. Sci. Comput. 19 (1) (2003) 95–122.
[39] A. Almansa, C. Ballester, V. Caselles, G. Haro, A TV based restoration model with local constraints, J. Sci. Comput. 34 (3) (2008) 209–236.
[40] T.H. Ma, T.Z. Huang, X.L. Zhao, New regularization models for image denoising with a spatially dependent regularization parameter, Abstr. Appl. Anal. (2013) http://dx.doi.org/10.1155/2013/729151.
[41] Y.Q. Dong, M. Hintermüller, M.M. Rincon-Camacho, Automated regularization parameter selection in multi-scale total variation models for image restoration, J. Math. Imaging Vision 40 (1) (2011) 82–104.
[42] K. Bredies, Y.Q. Dong, M. Hintermüller, Spatially dependent regularization parameter selection in total generalized variation models for image restoration, Int. J. Comput. Math. 90 (1) (2013) 109–123.
[43] M. Hintermüller, M.M. Rincon-Camacho, Expected absolute value estimators for a spatially adapted regularization parameter choice rule in L1-TV-based image restoration, Inverse Problems 26 (8) (2010) 85005–85034.
[44] H.Y. Liao, F. Li, M.K. Ng, Selection of regularization parameter in total variation image restoration, J. Opt. Soc. Amer. A 26 (11) (2009) 2311–2320.
[45] Y.W. Wen, R.H. Chan, Parameter selection for total-variation-based image restoration using discrepancy principle, IEEE Trans. Image Process. 21 (4) (2012) 1770–1781.
[46] A.Z. Chen, X.M. Huo, Y.W. Wen, Adaptive regularization for color image restoration using discrepancy principle, in: IEEE International Conference on Signal Processing, Communication and Computing, 2013, pp. 1–6.
[47] O. Michael, N. Bouguila, D. Arnold, Optimal selection of regularization parameter in total variation method for reducing noise in magnetic resonance images of the brain, Biomed. Eng. Lett. 4 (1) (2014) 80–92.
[48] G.H. Golub, M. Heath, G. Wahba, Generalized cross-validation as a method for choosing a good ridge parameter, Technometrics 21 (2) (1979) 215–223.
[49] S. Boyd, N. Parikh, E. Chu, B. Peleato, J. Eckstein, Distributed optimization and statistical learning via the alternating direction method of multipliers, Found. Trends Mach. Learn. 3 (1) (2011) 1–122.
[50] T . Goldstein, O.B., S. Setzer, Fast alternating direction optimization methods, SIAM J. Imaging Sci. 7 (3) (2014) 1588–1623.
[51] S. Wang, T.Z. Huang, X.L. Zhao, G. Liu, Y.G. Cheng, Double reweighted sparse regression and graph regularization for hyperspectral unmixing, Remote Sens. 10 (7) (2018) 1046.
[52] D.P. Bertsekas, A. Nedic, A.E. Ozdaglar, Convex analysis and optimization, Athena Sci. 129 (2) (2012) 420–432.
[53] T.H. Ma, T.Z. Huang, X.L. Zhao, Spatially dependent regularization parameter selection for total generalized variation-based image denoising, J. Comput. Appl. Math. (2016) 1–20, http://dx.doi.org/10.1007/s40314--016--0342--8.
[54] D.L. Donoho, I.M. Johnstone, G. Kerkyacharian, D. Picard, Wavelet shrinkage: Asymptopia, J. R. Stat. Soc. 57 (2) (1995) 301–369.
[55] W. Zuo, Z. Lin, A generalized accelerated proximal gradient approach for total variation based image restoration, IEEE Trans. Image Process. 20 (10) (2011) 2748–2759.
[56] Y.L. Wang, J.F. Yang, W.T. Yin, Y. Zhang, A new alternating minimization algorithm for total variation image reconstruction, SIAM J. Imaging Sci. 1 (3) (2008) 248–272.
[57] R.W. Liu, L. Shi, W. Huang, J. Xu, S.C. Yu, D. Wang, Generalized total variation-based MRI rician denoising model with spatially adaptive regularization parameters, Magn. Reson. Imaging 32 (6) (2014) 702–720.